ACS Catalysis

pubs.acs.org/acscatalysis

Research Article

Oxygen Evolution Activity on NiOOH Catalysts: Four-Coordinated Ni Cation as the Active Site and the Hydroperoxide Mechanism

Li-Fen Li, Ye-Fei Li,* and Zhi-Pan Liu*

Cite This: *ACS Catal.* 2020, 10, 2581−2590

Read Online

ACCESS | Metrics & More | Article Recommendations | Supporting Information

ABSTRACT: The NiOOH catalyst as obtained dynamically from electrodeposition of Ni^{2+}(aq) in the borate-containing electrolyte was observed to exhibit much higher oxygen evolution activity at a near-neutral pH range (7−9) compared to other NiO_x-based materials. Here, we demonstrate that this intriguing high activity is owing to the high concentration of Ni cationic vacancy on the nascent ultra-small NiOOH particles (<3 nm). By using first-principles calculations, we compute the thermodynamics of Ni dissolution and clarify the mechanism of oxygen evolution reaction (OER) on the γ-NiOOH surface. We show that (i) ∼4% Ni cations on the surface of γ-NiOOH dissolve at pH = 7 and 1.73 V versus reversible hydrogen electrode; (ii) on the pristine γ-NiOOH surface, OER proceeds via the "lattice peroxide" mechanism ($*H_2O \rightarrow *OH \rightarrow *O{-}O^{latt}H* \rightarrow O{-}O^{latt} \rightarrow O_2$) with an overpotential of 0.70 V; (iii) in the presence of Ni cationic vacancies, OER proceeds via the "hydroperoxide" mechanism ($*OH + *H_2O \rightarrow *2OH \rightarrow *OOH \rightarrow O_2$) with an overpotential of 0.40 V. Our electronic structure and geometrical structure analyses demonstrate that the structural flexibility at the four-coordinated Ni site nearby Ni vacancy, featuring the ability to bind two terminal oxo species, is key to boost the activity. Considering the presence of the active OOH intermediate, our theory thus implies that the ultra-small oxide nanoclusters with ample cation vacancies could be a paradigm in catalyst design for oxidation reactions.

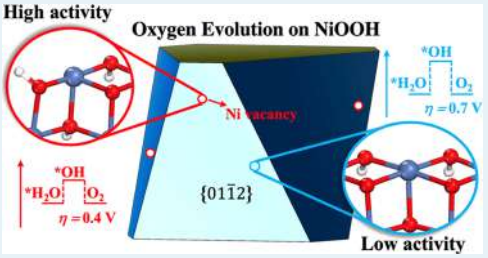

KEYWORDS: *oxygen evolution reaction, nickel oxyhydroxide, cationic vacancy, self-healing, DFT*

1. INTRODUCTION

Catalytic water splitting is an appealing and sustainable strategy to utilize electric (and solar) energy, where the development of robust and efficient catalysts for oxygen evolution reaction (OER) is a key obstacle. Among the candidates examined so far, nickel oxyhydroxide[1−6] (NiOOH) is perhaps one of the most popular materials because this nonprecious material (with appropriate synthetic modifications and at optimal reaction conditions) can approach high OER activity comparable to the industrial noble metal oxides, RuO_x and IrO_x.[3−6] For instance, under electrochemically cyclic voltammetry conditions, Pt-doped NiOOH exhibits a progressively increased OER activity as the number of cycle increases, and finally reaches an overpotential of 358 mV at 10 mA/cm^2.[7] Besides, the Fe-doped NiOOH is reported as another promising active anode for OER with a low overpotential of 280 mV at 10 mA/cm^2.[3−6,8]

Despite these advances, one of the key problems for the Ni-based catalyst remains: NiOOH can be stable and active only under a strong alkaline condition, pH ≈ 14,[8] which makes it difficult to couple with the hydrogen evolution reaction on the cathode that achieves the highest activity only under neutral or acidic conditions.[9−11] Recently, Bediako et al.[12] reported that the electrodeposited NiO_x obtained from Ni^{2+}(aq) solution containing the borate electrolyte (denoted as NiB_i) can be a good OER catalyst down to the near-neutral pH (7−9) that has a low overpotential of ∼425 mV at a current density of 1 mA/cm^2.[13] X-ray absorption spectroscopy reveals that the as-deposited NiB_i has a β-NiOOH structure, which appears to transform further into γ-NiOOH at the anodized potential (>1 V vs NHE), and the γ-NiOOH phase is believed as the true active phase for OER.[12,14] Paradoxically, NiOOH synthesized by mixing $Ni(NO_3)_2{\cdot}6H_2O$ and KOH shows no OER activity when pH < 11.[15] NiB_i is different from the conventional NiOOH in the so-called "self-healing" ability, that is, the dissolved Ni^{2+}(aq) can redeposit onto the NiOOH surface dynamically with the assistance of borate.[15,16] It implies that the self-healing process not only recovers the catalyst but should also play important roles in the activity of NiB_i under near-neutral conditions. Furthermore, not limited to Ni, the enhanced OER activity has also been reported in electrodeposited CoOOH obtained from Co^{2+}(aq) solution containing a phosphate electrolyte (CoP_i),[17] suggesting the general significance for understanding the relationship between the self-healing process and the OER activity.

Received: November 17, 2019
Revised: December 26, 2019
Published: January 24, 2020

https://dx.doi.org/10.1021/acscatal.9b04975
ACS Catal. 2020, 10, 2581−2590

Considering the mechanism of the self-healing process, we may expect that the enhanced OER activity should be related to the Ni cationic vacancies on the NiOOH surface. Indeed, some evidence emerges from the experiment recently. Zhao et al. reported that Ni vacancy in the ultrafine NiO nanosheets is essential for OER activity.[18] The increase of the Ni vacancy concentration in α-$Ni(OH)_2$ can reduce the OER overpotential by up to 0.31 V.[19]

The specific active site for OER on NiOOH is still under debate. It is generally believed that the active site for OER on NiOOH is the five-coordinated Ni sites on the $\{01\bar{1}N\}$ family (N represents any numbers)[20−24] because the set of surfaces contain unsaturated Ni sites and have the lowest surface energy apart from {0001} surfaces.[25] However, four-coordinated Ni sites have also been recently suggested to be the likely OER active site for NiOOH by experiments.[26] The four-coordinated Ni can be produced either at the edges of NiOOH particles or around the surface cationic vacancy. Therefore, evaluating the OER activity on the defective NiOOH surface is highly intriguing.

In this work, we aim to provide insights into the self-healing enhanced OER activity over the Ni-based catalyst. By using first-principles calculations, we first explore the energetics of OER on the pristine γ-NiOOH. Next, we evaluate the formation free energy of Ni vacancy at various sites. The OER activity around the most stable Ni vacancy is then estimated. For completeness of the understanding of OER on NiOOH, we also investigate the OER profiles on β-NiOOH because it is the precursor of γ-NiOOH and may also participate in the OER. Based on the results of both β-NiOOH and γ-NiOOH, the origin of the self-healing enhanced OER activity is revealed.

2. METHODOLOGY

2.1. Computational Models. β-NiOOH is a layered structure consisting of NiO_2 layers and intercalated protons. The average oxidation state (OS) of Ni ions in β-NiOOH is +3. On the other hand, the precise structure of γ-NiOOH is not well known because of the poor quality of X-ray diffraction data.[1−6] It is known that γ-NiOOH comprises NiO_2 layers, where protons, water molecules, and alkali cations are intercalated between the layers, but the configuration of the intercalated species has not been determined yet. The intercalated species modulate the average OS of Ni to around +3.66.[1]

To model the structure of the γ-NiOOH bulk phase, we use a deprotonating β-NiOOH structure to represent γ-NiOOH. In this model, 3/4 protons in the β-NiOOH are removed, and the average OS for Ni is +3.75. This model captures the known OSs and the local binding environment of Ni sites but neglects the role of intercalated species that have not been well characterized experimentally. A similar model has been used by Friebel et al. in the study of Fe-doped γ-NiOOH,[1] and their results show that the calculations based on the simplified model can yield the overpotential comparable with the experimental data.[1] Because the NiO_2 sublattice has a symmetry group of $R\bar{3}m$, in the following, we will use Bravais−Miller indices and Weber indices to denote the orientations of lattice planes and lattice directions for both γ-NiOOH and β-NiOOH.

We utilized a slab model of the (2×1) supercell (~4.84 Å × 12.06 Å) to simulate the $(01\bar{1}2)$ surface of γ-NiOOH and β-NiOOH. The slab model of γ-NiOOH is shown in Figure 1,

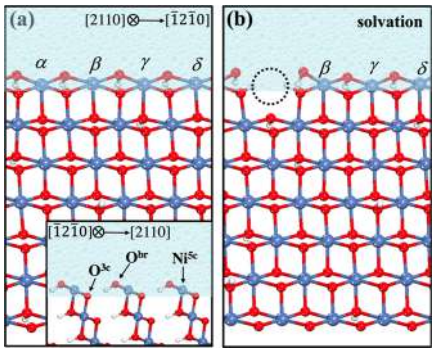

Figure 1. Atomic structures of (a) pristine and (b) defective γ-NiOOH $(01\bar{1}2)$ surfaces viewed from γ-NiOOH [2110]. The black dotted cycle highlights the cationic vacancy in the first Ni layer. We label the four reactive Ni sites in the unit cell as α, β, γ, and δ, respectively. The inset in (a) is a side view of the surface. The solvation effect was modeled by a periodic continuum solvation model with modified Poisson−Boltzmann equation (CM-MPB),[30−33] as schematically shown in figures by the azury shading in the vacuum region above the surface. Ni^{5c} represents five-coordinated Ni cation; O^{br} the bridging O anion; and O^{3c} the three-coordinated O anion. Indigo balls: Ni; red balls: O; and white balls: H.

while the model of β-NiOOH can be found in the Supporting Information. The top surface in a unit cell exposes four five-coordinated Ni cations, four bridging O anions, and four three-coordinated O anions (as indicated by Ni^{5c}, O^{br}, and O^{3c} in the inset of Figure 1a). We label the four reactive Ni sites in the unit cell as α, β, γ, and δ, respectively. On both γ-NiOOH and β-NiOOH surfaces, the O^{br} anions prefer to be protonated to form $*O^{br}H$ at the electrode potential (U) < 2.3 V versus reversible hydrogen electrode (RHE). The whole slab consists of seven Ni layers, and each Ni layer is defined as a horizontal Ni chain in Figure 1. The bottom two Ni layers together with the connected lattice O and H atoms are fixed in their bulk positions.

2.2. Calculation Details. All density functional theory (DFT) calculations were carried out within the periodic plane wave framework as implemented in Vienna Ab initio Simulation Package.[27] The electron−ion interaction was represented by the projector augmented wave, and the kinetic energy cutoff of the plane wave was set as 400 eV. The k-point mesh utilized was up to $(4 \times 4 \times 4)$ for bulk and $(3 \times 1 \times 1)$ for slab models in the Monkhorst−Pack scheme, which was verified to be accurate enough for these systems. The geometry convergence criterion was set as 0.08 eV/Å for the maximal component of force. Transition states of the O−O coupling were determined using the Dimer method.[28,29]

The previous studies have shown that the Hubbard term corrected DFT functional, PBE + U,[34,35] is sufficient to generate reliable geometry and OS of NiOOH,[36] but not accurate in describing the electronic structure, in particular for the band structures. The hybrid functional, such as HSE06, can improve the description of the electronic structure for NiOOH.[36] Following the recent studies,[36,37] both PBE + U and HSE06 (with PBE + U structures) calculations were performed in this work for computing the OER energy profile, and we show that a consistent picture for self-healing enhanced OER activity can be achieved, not sensitive to the DFT functional utilized. The effective value for Hubbard terms (U_{eff}) were set as 5.5 eV for Ni according to the linear response approach.[20,38,39] For all systems, the spin-polarization has been

https://dx.doi.org/10.1021/acscatal.9b04975
ACS Catal. 2020, 10, 2581−2590

considered to identify the true ground state electronic configuration. For the γ-NiOOH/β-NiOOH bulk, the spin ordering in the ground state is ferromagnetic within the NiO_2 sheets but antiferromagnetic between them, consistent with our previous studies.[20,40]

The solvation effect due to the long-range electrostatic interaction was modeled by a periodic continuum solvation model with modified Poisson−Boltzmann equation (CM-MPB).[32,41,42] The computational hydrogen electrode (CHE) approach is utilized to assess the thermodynamics of OER on both γ-NiOOH and β-NiOOH surfaces, which estimates the electrochemical potential of H^+ and e^- pair via the electrochemical equilibrium in standard hydrogen electrode (SHE), which is

$$\mu[H^+] + \mu^{SHE}[e^-] = 1/2G^\circ[H_2] \quad (1)$$

$\mu[H^+]$ is the electrochemical potential of a proton; $G^\circ[H_2]$ the standard Gibbs free energies of hydrogen; $\mu^{SHE}[e^-]$ the electrochemical potential of an electron in SHE. The detailed description of the CHE approach can be found in the Supporting Information and our previous papers.[43]

All the reported free energy changes in OER refer to the electrode potential (U) at 1.23 V versus RHE. With RHE metric, the effect of pH on the energetic profiles of OER vanishes.

3. RESULTS

In this section, we explore the thermodynamics of Ni dissolution and the influence of Ni vacancy on the OER activity. We have computed the OER profiles on both γ-NiOOH and β-NiOOH surfaces, and the results show that the trends of OER activity on both surfaces are the same. In this section, we will focus on the OER on the γ-NiOOH, while the results on β-NiOOH are listed in the Supporting Information and will be discussed in Section 4.1.

3.1. Surface Structures of γ-NiOOH in Aqueous Surroundings. It is known that the applied electrode potential will determine the surface status (species and coverage), which will then affect OER activity. In this regard, we need to first resolve the active surface for the electrode in the potential region of OER. We have constructed the surface Pourbaix diagram from the first-principles thermodynamics, as shown in Figure 2, and the calculation procedure is detailed in the following.

We first investigate the configuration of H_2O adsorption on the pristine γ-NiOOH surface without applied potential. Our results show that the H_2O molecules prefer to adsorb on the surface molecularly, which is at least 0.05 eV more stable than the dissociated configuration on all possible coverages. Hereinafter, we only consider the molecular adsorption configuration of H_2O.

For $*H_2O$ coverage, it can be estimated from the free energy change of the following reaction

$$H_2O(aq) + *nH_2O \rightarrow *(n+1)H_2O \quad (2)$$

and

$$\Delta G = G(*(n+1)H_2O) - G(*nH_2O) - G(H_2O(aq)) \quad (3)$$

$H_2O(aq)$ represents a H_2O molecule in aqueous solution, * represents the Ni^{5c} site, and n is the number of H_2O molecules in the unit cell. Because each unit cell involves four reactive

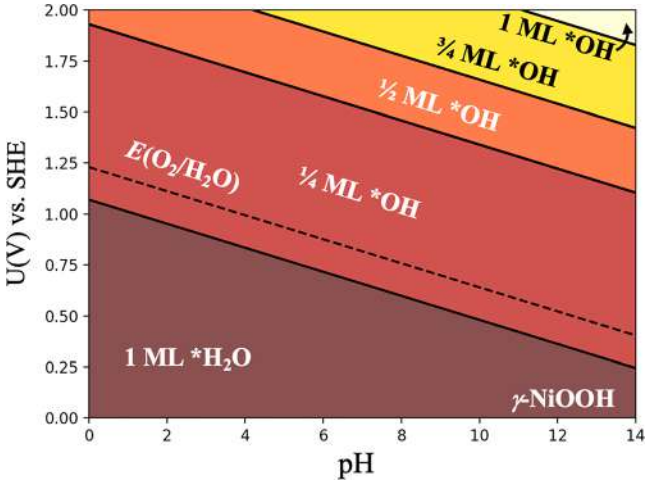

Figure 2. Surface Pourbaix diagram for the pristine γ-NiOOH $(01\bar{1}2)$. U is the electrode potential relative to SHE. The oblique dashed line represents the reversible potential of OER.

Ni^{5c} sites in our model (see Figure 1a), $*4H_2O$, $*3H_2O$, $*2H_2O$, and $*1H_2O$ correspond to 1 monolayer (ML), 3/4 ML, 1/2 ML, and 1/4 ML $*H_2O$ coverages, respectively. From our calculations, the 1 ML $*H_2O$ covered surface is the most stable phase in aqueous solution for γ-NiOOH. For example, on the 3/4 ML $*H_2O$-covered surface, it is exothermal by 0.24 eV if adsorbing further H_2O molecules to reach 1 ML $*H_2O$. Once H_2O coverage is 1 ML, the additional H_2O adsorption becomes thermodynamically unfavorable, endothermic by 0.39 eV at 1.25 ML.

With an applied potential, $*H_2O$ may decompose to *OH, by the reaction $*H_2O \rightarrow *OH + H^+(aq) + e^-$. According to the CHE approach, the free energy change is defined as

$$\Delta G = G[*OH] + 1/2G[H_2] - G[*H_2O] - 0.059*pH - |e|U \quad (4)$$

where U is the electrode potential relative to SHE, and the term $-0.059*pH$ is the effect of pH on the ΔG at a pH different from 0. The Pourbaix diagram can finally be determined by the minimization of the Gibbs free energy among a set of surface configurations relevant for OER, which reveals the thermodynamically most stable structure of the catalyst surface for a given electrode potential and pH values.

The calculated Pourbaix diagram of γ-NiOOH $(01\bar{1}2)$ in Figure 2 shows that the surface status varies from 1 ML $*H_2O$ to 1/4 ML to 1/2 ML to 3/4 ML to 1 ML *OH progressively as the electrode potential increases. At pH = 7 and U = 0.82 V (the reversible potential of OER at pH = 7), we found that the most stable phase is 1/4 ML *OH. Therefore, we will use 1/4 ML *OH as the initial state for OER on the pristine γ-NiOOH.

3.2. Mechanism and Activities of OER on γ-NiOOH. Now, we are at the position to compare the OER activities on γ-NiOOH with and without cationic vacancy, which is critical to understand the origin for the self-healing enhanced OER activity. Toward this goal, we start by investigating the activity of OER on the pristine γ-NiOOH. Here, we consider three likely reaction pathways, namely, the "lattice peroxide" path:[30] $*H_2O \rightarrow *OH \rightarrow *O{-}O^{latt}H \rightarrow *O{-}O^{latt} \rightarrow O_2$, the "hydroperoxide" path:[44] $*OH + *H_2O \rightarrow *2OH \rightarrow *OOH \rightarrow O_2$, and the "electrochemical metal peroxide" path:[44,45] $*H_2O$

https://dx.doi.org/10.1021/acscatal.9b04975
ACS Catal. 2020, 10, 2581−2590

→ *OH → *O → *OOH → O_2. The elementary reactions involved are depicted in the following.

The "lattice peroxide" path

$$*H_2O + *O^{latt}H \rightarrow *OH + *O^{latt}H + H^+(aq) + e^- \quad (5)$$

$$*OH + *O^{latt}H \rightarrow *O - O^{latt}H + H^+(aq) + e^- \quad (6)$$

$$*O - O^{latt}H \rightarrow *O - O^{latt} + H^+(aq) + e^- \quad (7)$$

$$*O - O^{latt} + 2H_2O(l) \rightarrow *H_2O + *O^{latt}H + O_2(g) + H^+(aq) + e^- \quad (8)$$

The "hydroperoxide" path

$$*OH + *H_2O \rightarrow *2OH + H^+(aq) + e^- \quad (9)$$

$$*2OH \rightarrow *OOH + H^+(aq) + e^- \quad (10)$$

$$*OOH + 2H_2O(l) \rightarrow *2H_2O + O_2(g) + H^+(aq) + e^- \quad (11)$$

$$*2H_2O \rightarrow *OH + *H_2O + H^+(aq) + e^- \quad (12)$$

The "electrochemical metal peroxide" path

$$*H_2O \rightarrow *OH + H^+(aq) + e^- \quad (13)$$

$$*OH \rightarrow *O + H^+(aq) + e^- \quad (14)$$

$$*O + H_2O(l) \rightarrow *OOH + H^+(aq) + e^- \quad (15)$$

$$*OOH + H_2O(l) \rightarrow *H_2O + O_2(g) + H^+(aq) + e^- \quad (16)$$

In the equations, the O^{latt} indicates the lattice O, defined as the O atom bond with at least two Ni ions, for example,, O^{br} and O^{3c} in Figure 1. All mechanisms comprise four successive proton-coupled electron transfer (PCET) steps. By following the above mechanisms, we have explored the lowest energy pathways on the (defected) NiOOH catalyst. For each intermediate state, we have considered several possible configurations to ensure that the most stable configuration is identified.

3.3. OER on the Pristine γ-NiOOH. The lowest energy pathway on pristine γ-NiOOH follows the "lattice peroxide" mechanism. The reaction network for OER on the pristine γ-NiOOH is shown in Figure 3. The key reacting species (i.e., proton and $*O^{br}O$) that will be released from the surface in the subsequent step are highlighted using green and yellow cycles. The formula of the elementary steps, as well as the corresponding free energy changes, is listed in Table 1. The elementary steps involving electrons (e^-) indicate that this step is an electrochemical step, in which the free energy change depends on the electrode potential.

At the initial state (**state 1**, Figure 3), the γ-NiOOH surface is covered by 1/4 ML *OH, where Ni^{5c} at the δ site is covered by OH and other three Ni^{5c} ions are covered by three H_2O molecules in each unit cell. Because the OS of Ni ions may vary among Ni(II), Ni(III), and Ni(VI) in oxides, it is intriguing for us first to investigate the OS of Ni^{5c} ions. To this end, we take a close look at the onsite spins of these Ni^{5c} ions in **state 1**, which can represent their OS. Our results show that Ni^{α} and Ni^{γ} have magnetic moments of 1.59 μ_B and 1.44 μ_B, while Ni^{β} and Ni^{δ} have lower magnetic moments of 1.11 μ_B and 0.10 μ_B, respectively. From the electronic configuration of $Ni^{(2+n)+}$, that is, $t_{2g}^6 e_g^{2-n}$ in the octahedral ligand field, Ni(IV) has zero net spin, and only the OS within Ni(II) to Ni(III) are spin-polarized with a net magnetic moment.[37] (cf. 1.22 μ_B for Ni(III) in bulk β-NiOOH and 1.77 μ_B for Ni(II) in bulk β-$Ni(OH)_2$ by PBE + *U*). With the onsite spins, we can derive that the OS of Ni^{α} and Ni^{γ} are between Ni(II) and Ni(III) states [denoted as Ni(II/III)], while Ni^{β} is Ni(III) and Ni^{δ} is Ni(IV). In agreement with the OS difference, we noticed that Ni^{β} exhibits a Jahn−Teller effect with the axial Ni−O bond lengthened to 2.06 Å, longer than the four equatorial Ni−O bonds (1.90 Å).

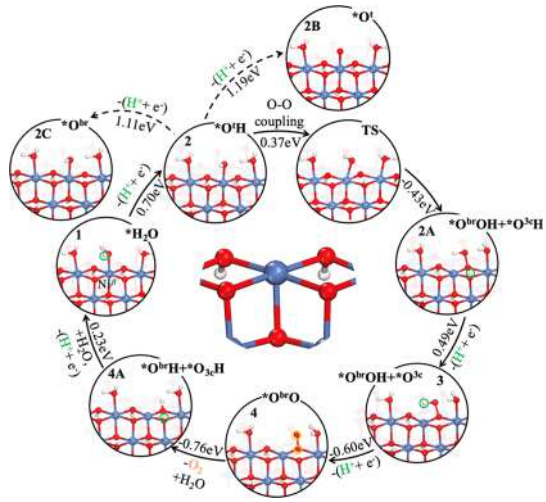

Figure 3. Reaction network for OER on pristine γ-NiOOH ($01\bar{1}2$). The solid path denotes the mechanism of OER, where **state 1** is the initial state. The end-on dashed path indicates this pathway is blocked because of the high free energy cost. The small green or yellow cycles highlight the proton or O_2 that would be released from the surface in the subsequent step. The translucent atoms belong to the adjacent NiOOH layer. The energy beside each arrow represents the corresponding free energy change by PBE + *U*. The bold free energy change indicates that this step is rate-determining. The local environment of the reactive Ni^{5c} site is highlighted in the center of the figure. Indigo balls: Ni; red balls: O; white balls: H.

In the first PCET step, a proton of the adsorbed $*H_2O$ molecule atop the reactive Ni^{β} ion is released into the solution (see **1** → **2**), leading to an *OH ($*O^tH$). This step is exothermic by 0.70 eV.

In the second PCET step, the $*O^tH$ reacts with an adjacent bridging OH ($*O^{br}H$), which generates an $*O^{br}OH$ by releasing the proton of $O^{br}H$ to the solution (see **2** → **3**). This step is endothermic by 0.43 eV. $*O^{br}OH$ in **state 3** belongs to O_2^{2-} peroxide in the lattice, as seen from a bond distance of 1.45 Å (a typical bond length for peroxide) and the zero magnetic moment. This reaction involves two elementary steps. First, the $*O^tH$ bonds with $*O^{br}H$ to form an $*O^{br}-O$ bond, and meanwhile, the proton of $*O^{br}H$ passes to the nearby $*O^{3c}$. This reaction is exothermic by 0.06 eV (see **2** → **2A**), with a reaction barrier of 0.37 eV (see **2** → **TS**). Second, the proton of $*O^{3c}H$ is removed from the surface (see **2A** → **3**), which is endothermic by 0.49 eV.

In the third PCET step, the proton of the $*O^{br}OH$ is released into the solution (see **3** → **4**). The generated $*O^{br}O$ is superoxide, evident from a O−O distance of 1.32 Å and a magnetic moment of ∼1 μ_B. This step is exothermic by 0.60 eV.

https://dx.doi.org/10.1021/acscatal.9b04975
ACS Catal. 2020, 10, 2581−2590

Table 1. Free Energy Changes (ΔG, in eV) of Each Elementary Step by PBE + U and HSE06 Functionals

elementary step	ΔG_{PBE+U} (ΔG_{HSE06})	ΔE_{PBE+U} [b]
Pristine		
1 → 2: $*H_2O \rightarrow *O^tH + H^+(aq) + e^-$	**0.70**(0.65)[a]	2.30
2 → 2A: $*OH^t + *O^{br}H + *O_{3c} \rightarrow *O^{br}OH + *O_{3c}H$	−0.06(0.16)	−0.13
2 → TS: $*OH^t + *O^{br}H + *O_{3c} \rightarrow TS$	0.37(0.18)	0.37
2A → 3: $*O^{3c}H \rightarrow *O^{3c} + H^+(aq) + e^-$	0.49(**0.81**)	2.07
3 → 4: $*O^{br}OH \rightarrow *O^{br}O + H^+(aq) + e^-$	−0.60	1.09
4 → 4A: $*O^{br}O + H_2O(l) + *O^{3c} \rightarrow O_2(g) + *O^{br}H + *O^{3c}H$	−0.76	−1.58
4A → 1: $*O^{3c}H + H_2O(l) \rightarrow *H_2O + *O^{3c} + H^+(aq) + e^-$	0.23	1.83
w. vac.		
1 → 2: $*H_2O^t + *OH \rightarrow *O^tH + *OH + H^+(aq) + e^-$	**0.40**(**0.43**)	2.00
2 → 2A: $*O^tH + *OH + *O^{br} \rightarrow *OOH + *O^{br}H$	−0.20(−0.20)	0.23
2 → TS: $*O^tH + *OH + *O^{br} \rightarrow TS$	0.54(0.25)	0.54
2A → 3: $*O^{br}H \rightarrow *O^{br} + H^+(aq) + e^-$	0.28(0.00)	1.86
3 → 4: $*OOH \rightarrow *OO + H^+(aq) + e^-$	−0.42	1.18
4 → 4A: $*OO + 2H_2O \rightarrow O_2(g) + *2H_2O$	0.04	−0.78
4A → 1: $*2H_2O \rightarrow *H_2O^t + *OH + H^+(aq) + e^-$	−0.11	1.49

[a]The bold free energy change indicates this step is rate-determining. [b]ΔE is the total energy change directly from DFT calculations at U = 0 V.

Finally, in the fourth PCET step, $*O^{br}O$ desorbs from the lattice site and the surface recovers initial **state 1** (see **4 → 1**). This reaction is exothermic by 0.53 eV and consists of two elementary steps. First, $*O^{br}O$ desorbs from the lattice to generate an O_2 molecule. At the same time, a H_2O molecule dissociates on the lattice site previously occupied by $*O^{br}O$, producing a new $*O^{br}H$ and an $*O^{3c}H$ (see **4 → 4A**). This step is exothermic by 0.76 eV. Second, the proton of $*O^{3c}H$ is released into the solution, and another H_2O molecule attaches on top of bare Ni^{5c} to recover initial **state 1** (see **4A → 1**). This reaction is endothermic by 0.23 eV. Altogether, our calculations show that the rate-determining step is the first PCET step (**1 → 2**), which requires an overpotential of 0.70 V.

For comparison, we compute the energetic profiles of the first three elemental steps (i.e., **1 → 2 → 2A → 3**) by HSE06 functional, and the results are listed in Table 1. We note that the free energy difference up to 0.32 eV may exist in a single elementary step (e.g., **2A → 3**) between PBE + U and HSE06 functionals. We have carefully examined the setup of our calculations, and confirm that this difference is indeed caused by the different functionals we used. HSE06 functional results yield the rate-determining step at **2A → 3**, with a higher overpotential of 0.81 V. The experimental overpotential of NiOOH being around 0.5−0.6 V[8] suggests that the overpotential obtained from PBE + U is in better agreement with the experiment than HSE06.

3.4. Location of Ni Vacancy. Before we investigate the OER on the defective γ-NiOOH surface, we need to determine the location of Ni vacancy. It is known that under neutral pH conditions, NiOOH is not stable thermodynamically: the Ni cation of the oxide can dissolve as $Ni^{2+}(aq)$ leaving from the surface.[46] The possible reactions for treating the surface Ni dissolution equilibrium can be described as eqs 17−20

$$*(\text{oxide}) + 3H^+(aq) + e^- \rightarrow *\square\text{-}3H(\text{oxide}) + Ni^{2+}(aq) \quad (17)$$

$$*(\text{oxide}) + 2H^+(aq) \rightarrow *\square\text{-}2H(\text{oxide}) + Ni^{2+}(aq) \quad (18)$$

$$*(\text{oxide}) + H^+(aq) \rightarrow *\square\text{-}H(\text{oxide}) + Ni^{2+}(aq) + e^- \quad (19)$$

$$*(\text{oxide}) \rightarrow *\square(\text{oxide}) + Ni^{2+}(aq) + 2e^- \quad (20)$$

where *(oxide) represents the pristine γ-NiOOH surface and $*\square$ represents the cationic vacancy. In the reactions (17−19), protons in the solution adsorb [$3H^+(aq)$, $2H^+(aq)$, and $1H^+(aq)$] on the dangling O species around the vacancy to stabilize the remaining γ-NiOOH slab. In our simulation, we have considered all the possible surface compositions with and without Ni vacancy, including 1 ML $*H_2O$, 1/4 ML *OH (on the pristine γ-NiOOH surface), $*\square$-3H, $*\square$-2H, $*\square$-H, and $*\square$ (on the defective γ-NiOOH surface). For instance, Figure 4 shows the thermodynamics phase diagram for a surface Ni

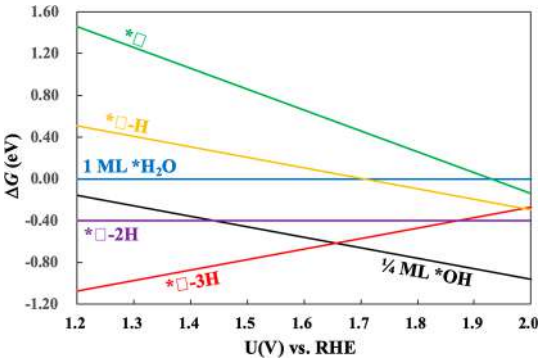

Figure 4. Phase diagram of 1/4 ML *OH (black line), 1 ML $*H_2O$ (blue line) on the pristine γ-NiOOH surface, and $*\square$-3H (red line), $*\square$-2H (purple line), $*\square$-H (yellow line), and $*\square$ (green line) on the defective γ-NiOOH surface with a surface Ni vacancy at pH = 7.

vacancy. The result shows that the $*\square$-3H surface phase is the most stable under OER conditions (<1.65 V vs RHE), indicating that the dangling O atoms (after Ni dissolution) are unstable at the potentials and can capture protons from the electrolyte. The same conclusion can also be derived for subsurface Ni vacancies. As a result, eq 17, an overall reduction reaction, occurs at the OER condition. The formation free energy of the Ni vacancy (ΔG_{vac}) is then defined as

$$\Delta G_{vac} = \mu[Ni^{2+}(aq)] + G(*\square\text{-}3H) - G(*) - 3\mu[H^+(aq)] - \mu[e^-] \quad (21)$$

https://dx.doi.org/10.1021/acscatal.9b04975
ACS Catal. 2020, 10, 2581−2590

To estimate ΔG_{vac}, we set pH = 7 and U = 1.32 V relative to SHE (corresponding to an overpotential of 0.5 V at pH = 7).

To simplify the ΔG_{vac} computation, we have recoursed to the standard half-electrode potential $E^{\circ}(Ni(s)/Ni^{2+})$ and standard molar Gibbs energy of formation $\Delta_f G^{\circ}(Ni(OH)_2(s))$ for computing the electrochemical potential of $Ni^{2+}(aq)$ in solution $\mu[Ni^{2+}(aq)]$ (which requires a statistical sampling for the ion in solution and thus is computationally extensive). The detailed description of this approach can be found in the Supporting Information. We set the concentration of Ni^{2+} ($c[Ni^{2+}]$) as 1×10^{-6} mol/L, a moderate concentration for a hydrated cation in solution.[46] The energetics of $Ni(OH)_2$ oxide (Brucite structure, $P\bar{3}m1$) is computed from PBE + U straightforwardly.[46]

Using eq 21, we investigate all the likely Ni cationic vacancies on the γ-NiOOH surface and subsurface, that is, the positions at the first, second, and third Ni layers in Figure 1. The favorable location for Ni vacancy is identified by comparing the ΔG_{vac}. On the surface, our results show that ΔG_{vac} at the Ni(II/III) site (i.e., Ni^{α}/Ni^{γ}) is 0.09 eV, while ΔG_{vac} at the Ni(III) site (i.e., Ni^{β}) is 0.23 eV. As to the subsurface sites, ΔG_{vac} at the second and third Ni layers are larger than 0.80 eV. Therefore, at the ambient condition, the formation of Ni vacancies occurs mostly at the surface Ni(II/III) sites. From thermodynamics, we can estimate that around 4.3% of surface Ni sites are dissolved into the solution.

3.5. OER on the Defective γ-NiOOH. In this section, we evaluate the OER activity on γ-NiOOH with a surface Ni(II/III) vacancy at the site α (see Figure 1b), the most stable configuration for Ni vacancy. On the defective surface, there are three possible reactive sites for OER, namely, Ni^{β}, Ni^{γ}, and Ni^{δ} (see Figure 1b). Both Ni^{β} and Ni^{δ} are the analogous four-coordinated Ni (Ni^{4c}) site that bonds with four lattice O (lattice O is defined as that bonds with at least two Ni ions) and an equatorial terminal *OH; Ni^{γ} is a Ni^{5c} site. In the presence of Ni vacancy, the onsite spins on Ni^{β}/Ni^{δ} and Ni^{γ} are 0.98 μ_B and 1.05 μ_B, respectively. We can, therefore, assign the formal OS of Ni^{β}, Ni^{γ}, and Ni^{δ} as Ni(III).

We have searched the lowest energy pathway for OER on Ni^{β}/Ni^{δ} and Ni^{γ}. The Ni^{β}/Ni^{δ} is often regarded as molecule-like site, due to the structural similarity to homogeneous $Ni^{2+}(aq)$ ions. Our results show that the Ni^{β}/Ni^{δ} site is more active than Ni^{γ}. In the following, we will focus on the OER on Ni^{β}. The lowest energy pathway on Ni^{β} follows the "hydroperoxide" mechanism, and the reaction network is shown in Figure 5.

In initial **state 1**, three H_2O molecules adsorb atop the Ni^{β}, Ni^{γ}, and Ni^{δ} sites, respectively. The OER begins with a PCET step of $*H_2O$ atop Ni^{β} ($*H_2O^t$), leading to an *OH standing on Ni^{β} ($*O^tH$, see **1** → **2**). This step is endothermic by 0.40 eV.

In the second PCET step, $*O^tH$ reacts with the equatorial *OH to generate an *OOH (see **2** → **3**). This step is endothermic by 0.08 eV. The generated *OOH is peroxide, as seen from the bond length (1.44 Å) and zero magnetic moment. This step comprises two elementary steps: first, the $*O^tH$ bonds with the equatorial *OH to form a hydroperoxide *OOH by passing the proton of *OH to a lattice $*O^{br}$. This step is exothermic by 0.20 eV (see **2** → **2A**), with a reaction barrier of 0.54 eV (see **2** → **TS**). Subsequently, the proton of $*O^{br}H$ is released into the solution (see **2A** → **3**), which is endothermic by 0.28 eV.

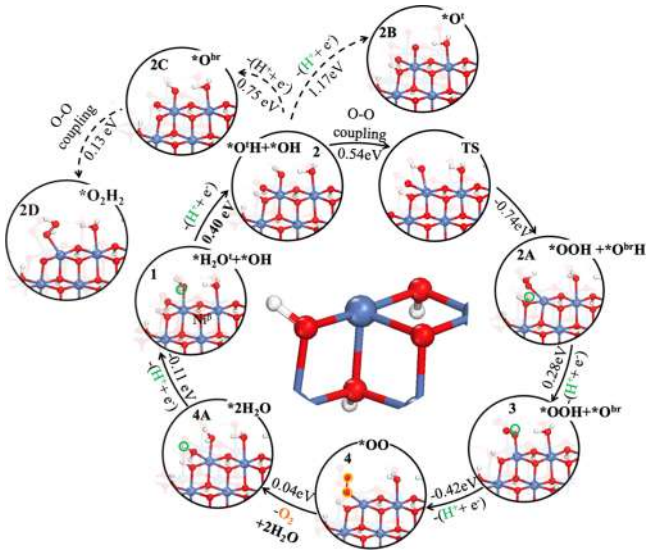

Figure 5. Reaction network for OER on the defective γ-NiOOH. The solid path denotes the mechanism of OER on the defective γ-NiOOH, where **state 1** is the initial state. The end-on dashed path indicates that this pathway is blocked because of the high free energy cost. The small green and yellow cycles highlight the proton or O_2 that would release from the surface in the subsequent step. The translucent atoms belong to the adjacent NiOOH layer. The chemical formula and the energy beside the arrow represent the variation of the chemical composition and the corresponding free energy change by PBE + U. The bold free energy change indicates that this step is rate-determining. The local environment of the reactive Ni^{4c} is highlighted in the center of the figure. Indigo balls: Ni; red balls: O; and white balls: H.

In the third PCET step, the proton of *OOH removes from the surface (see **3** → **4**), leaving an *OO on Ni^{β}. The O−O bond length is 1.26 Å and the magnetic moment on *OO is 1.3 μ_B. This step is exothermic by 0.42 eV. In the fourth PCET step, an O_2 molecule desorbs from the surface, and initial **state 1** is recovered (see **4** → **1**). This step is exothermic by 0.07 eV and comprises two elementary steps: first, an O_2 molecule desorbs from the surface, and two H_2O molecules adsorb on the Ni^{β} site. This step is endothermic by 0.04 eV. Second, the proton of the equatorial $*H_2O$ releases into the solution, with a free energy change of −0.11 eV.

Overall, the first proton releasing step (step **1** → **2**) is the rate-determining step on the defective γ-NiOOH surface, requiring an overpotential of 0.40 V. By comparing the OER energetic profiles between the defective and pristine γ-NiOOH, we show that the presence of Ni vacancy reduces the overpotential by 0.30 V (also see Table 1). Therefore, the surface Ni vacancy can promote OER on γ-NiOOH.

To ensure our conclusion, we use the hybrid HSE06 functional to recalculate the energetics of the first three elemental steps on the defective γ-NiOOH, and the results are listed in Table 1. The rate-determining step determined by the HSE06 functional is step **1** → **2**, consistent with the result from PBE + U. Furthermore, HSE06 predicts that the overpotential decreases from 0.81 to 0.43 V after introducing a surface Ni vacancy, which is also in agreement with the trend in PBE + U. Both PBE + U and HSE06 functionals thus demonstrate that the presence of Ni vacancy can improve the OER activity of γ-NiOOH.

https://dx.doi.org/10.1021/acscatal.9b04975
ACS Catal. 2020, 10, 2581−2590

4. DISCUSSIONS

4.1. Influence of the Active Phase of γ-NiOOH or β-NiOOH on the OER Activity. The X-ray absorption spectroscopy provides evidence that the as-deposited NiB_i has a β-NiOOH structure, which appears to transform further to γ-NiOOH in bulk under OER conditions.[12,14] However, whether the surface is a mixed phase with both β-NiOOH and γ-NiOOH remains unclear.

To clarify the puzzle, in this work, we have investigated the OER profiles on the β-NiOOH surface using the same theoretical approach reported above for γ-NiOOH. The results have been detailed in Figures S5 and S6. Here, we briefly overview the results. On the pristine β-NiOOH surface, the active site is Ni^{5c}, and OER proceeds via the "lattice peroxide" mechanism. The rate-determining step is the second PCET of $*O^tH + *O^{br}H \rightarrow *O^{br}OH + H^+(aq) + e^-$, with overpotentials of 0.63 V (with PBE + U) and 0.93 (with HSE06). While for the defective β-NiOOH (with surface Ni vacancy), the active site is Ni^{4c}, and the reaction occurs via the "hydroperoxide" mechanism. The rate-determining step is the first PCET of $*H_2O^t + *OH \rightarrow *O^tH + *OH + H^+(aq) + e^-$, with overpotentials of 0.30 V (with PBE + U) and 0.61 (with HSE06). Therefore, the presence of Ni vacancy on the β-NiOOH surface also benefits the OER activity.

Because β-NiOOH and γ-NiOOH results are similar, it is wondering why the activities on both phases are comparable. We show that both β-NiOOH and γ-NiOOH phases share a similar layered structure comprising NiO_2 sheets. The major structural difference between the two phases is the intercalated species that modulate the OS of Ni: In the β-NiOOH phase, the NiO_2 layers are intercalated with proton, while in the γ-NiOOH phase, NiO_2 layers are intercalated with protons, water molecules, and alkali cations. In our study, we always first consider the thermodynamics phase diagram for the surface. It turns out that at U = 1.23 V, β-NiOOH will be covered by 1 ML $*H_2O$ (see Figure S4), while γ-NiOOH is covered by 1/4 ML *OH. The electronic structures show that on the β-NiOOH surface, Ni^{α}, Ni^{β}, and Ni^{γ} have the magnetic moments of 1.62, 1.09, and 1.62 μ_B, which are quite similar to their counterparts, that is, 1.59, 1.11, and 1.44 μ_B, on γ-NiOOH. Therefore, we conclude that the difference in bulk between β- and γ-phases diminishes to the surface under the OER condition (i.e., above 1.23 V vs RHE), where the dynamics of adsorbed surface species bring to the similar OS of the exposed surface sites. This result, in fact, indicates that the surface states of the β-phase convert to those of γ-phases early, while the full conversion of the bulk phase to γ-phases should be much slower because of kinetics.

Based on the above calculations, we can conclude that: (i) the local structure of surface Ni ions is critical for OER. The active phase on the surface should be Ni^{4c}; (ii) for the investigation of an electrochemical process, it is critical to explore the thermodynamics phase diagram of the surface, which largely determines the local structure.

4.2. Origin of the Self-Healing Enhanced OER Activity. At this point, we have shown that the presence of surface cationic vacancy can promote the OER activity of both NiOOH phases, it is natural to wonder why. To clarify the origin of the different energetic profiles between the pristine and defective γ-NiOOH, we plot the total and projected density of states (TDOS and PDOS) of both surfaces in Figure 6. The TDOS shows that both pristine and defective γ-NiOOH have similar profiles. In particular, both surfaces have no band gap in the majority spin and a wide band gap (~2 eV) in the minority spin. Besides, the PDOS of the reactive Ni^{β} shows that the distributions of the states are comparable on both surfaces. For instance, the band centers of the unoccupied states on the pristine γ-NiOOH are 2.2 eV (in majority spin) and 3.6 eV (in minority spin) relative to the Fermi level, while they are 2.3 and 3.5 eV on the defective γ-NiOOH. Therefore, the reactive Ni^{β} sites on both surfaces share similar electronic structures.

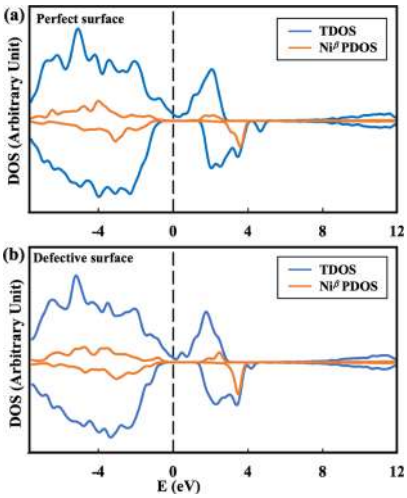

Figure 6. Electronic structures of γ-NiOOH surfaces (in **state 1**) by using the HSE06 functional. (a) Pristine γ-NiOOH and (b) defective γ-NiOOH. Blue lines: total density of states (DOS); orange lines: projected DOS of the reactive Ni^{β} site. In each panel, the DOS of both majority (up) and minority spins (down) are displayed. The magnitude of PDOS is amplified by 5 fold. The dashed line represents the Fermi level.

By ruling out the contribution from the electronic structures, we believe that the enhanced OER activity on the defective γ-NiOOH can be traced back to the local geometry of the reactive Ni^{β} sites. Specifically, on the pristine γ-NiOOH, the reactive Ni^{β} site bonds with five lattice O atoms (Ni^{5c}), and can only bond with one terminal oxo species (see $*O^tH$ state in Figure 3). While on the defective γ-NiOOH, the reactive Ni^{β} site coordinates with four lattice O atoms (Ni^{4c}) and thus is able to adsorb two terminal oxo species (see $*O^tH + *OH$ state in Figure 5). The different structural flexibilities between Ni^{5c} and Ni^{4c} may be the key to the different OER activities between pristine and defective γ-NiOOH.

In fact, the high activity of Ni^{4c} revealed from theory should be the direct cause for the experimental finding that NiO_x nanoparticles with smaller sizes exhibit higher OER activity than the bulk counterpart.[47] We note that the average particle size of active NiOOH in the NiB_i system is small, around 2 to 3 nm.[13,14,48,49] In contrast, the inactive NiOOH synthesized via a chemical approach (e.g., mixing $Ni(NO_3)_2{\cdot}6H_2O$ and KOH) has a larger particle size (>10 nm).[5]

We can now analyze the Ni^{4c} concentrations for γ-NiOOH particles from thermodynamics. Figure 7 illustrates the population of Ni^{4c} (N_{popu}) against the particle size (D, where $D = 2 \times \sqrt[3]{3V/4\pi}$ and V is the volume of the NiOOH nanoparticle) grows from 1 to 10 nm. N_{popu} is evaluated by eq 22

$$N_{popu} = N_{4c}/N_{tot} \quad (22)$$

https://dx.doi.org/10.1021/acscatal.9b04975
ACS Catal. 2020, 10, 2581−2590

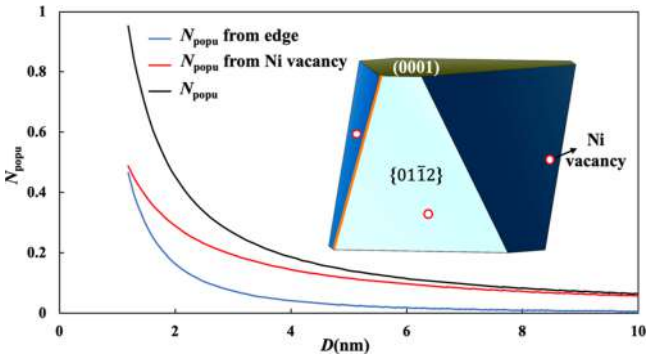

Figure 7. Population of Ni^{4c} vs γ-NiOOH particle size D. The black line is the overall population of Ni^{4c} (N_{popu}). The red line represents the N_{popu} contributed from the surface Ni vacancies (N_{popu} from Ni vacancy); the blue line the N_{popu} contributed from the edges (N_{popu} from edge). The inset is the Wulff shape of γ-NiOOH. The top surface with yellow color is (0001), and those with the (deep/light) blue color are $\{01\bar{1}2\}$. The red cycles are the surface Ni vacancies on $\{01\bar{1}2\}$. D defines the size of the γ-NiOOH particle. ($D = 2 \times \sqrt[3]{3V/4\pi}$, where V is the volume of the NiOOH nanoparticle).

where N_{4c} represents the number of Ni^{4c} sites; N_{tot} the total number of Ni atoms. The inset in Figure 7 is the Wulff shape of γ-NiOOH, which consists of {0001} and $\{01\bar{1}2\}$. The surface energies to construct the Wulff shape are listed in the Supporting Information. To calculate the surface energies of γ-NiOOH, we need to evaluate the surface area of a crystal plane correctly, which requires a crystal structure with right interlayer spacing. To this end, here we use a γ-NiOOH crystal structure which NiO_2 layers intercalated with Na^+ ions and H_2O (see Supporting Information for details) rather than the deprotonating β-NiOOH. This model has an interlayer spacing close to the experimental data (~7 Å).[1−6] The Ni^{4c} sites can arise from two sources: (i) the edges between two $\{01\bar{1}2\}$ surfaces (see the orange edge of the Wulff shape in Figure 7); (ii) the Ni vacancies on the $\{01\bar{1}2\}$ surfaces. We can estimate N_{4c} by eq 23.

$$N_{4c} = L \times \rho_L + 2S \times \rho_S \times \frac{\exp(-\Delta G_{vac}/k_B T)}{1 + \exp(-\Delta G_{vac}/k_B T)} \quad (23)$$

L is the length of edges between $\{01\bar{1}2\}$; ρ_L is the density of Ni at the edge; S is the surface area of $\{01\bar{1}2\}$; ρ_S is the density of Ni on $\{01\bar{1}2\}$; $\frac{\exp(-\Delta G_{vac}/k_B T)}{1+\exp(-\Delta G_{vac}/k_B T)}$ is the equilibrium concentration of Ni vacancy on $\{01\bar{1}2\}$. The factor 2 indicates that one Ni vacancy can produce two Ni^{4c} sites.

Figure 7 shows that as the particle size D grows, N_{popu} contributed from Ni vacancy becomes increasingly significant compared with the N_{popu} contributed from the edges (denoted as N_{popu} from Ni vacancy and N_{popu} from edge). This result can be understood by the slower decay of the specific surface area (in the order of D^{-1}) than the specific length of edges (in the order of D^{-2}). In particular, at 2 nm, the overall N_{popu} is around 0.44, and N_{popu} from Ni vacancy surpasses that from the edges. As the size increases to 10 nm, N_{popu} diminishes to below 0.06. Because the particle size in experiments is larger than 2 nm, the major source of Ni^{4c} should thus be the surface Ni vacancy on the γ-NiOOH particle. Overall, the relatively small γ-NiOOH particles expose a large specific surface area, which can provide a significant number of Ni vacancies on the surface at neutral pH conditions and benefit OER. As the particle size grows, the population of Ni^{4c} becomes deficient, which thus quenches the OER activity.

Based on the above analysis, we can finally understand the self-healing enhanced OER activity observed in experiments as follows. In the OER, the four-electron oxidation of water to oxygen is accompanied by the release of four protons. In near-neutral conditions, the NiOOH reacts with the released protons (acid), which leads to corrosion by the leaching of Ni ions and dissolution of the oxide. In the self-healing NiB_i, the dissolved $Ni^{2+}(aq)$ can redeposit onto the NiOOH surface with the assistance of borate. The equilibrium between dissolution and redeposition of Ni ions in NiB_i limits the size of γ-NiOOH to 2−3 nm. The ultra-small γ-NiOOH nanoparticles contain ample Ni^{4c} sites, which may act as the truly active catalyst for OER. Therefore, we can conclude that the ultra-small particle size in NiB_i may be the cause of self-healing enhanced OER activity.

Finally, we would like to comment on why the conventional NiOOH, that is, operated under strong alkaline conditions such as 0.1 M KOH, has low activity, as observed in the experiment.[1] From our results, the concentration of Ni vacancies is extremely low at pH ≈ 14 and U = 1.73 V versus RHE: only $\sim 10^{-14}$ Ni cations on the surface may dissolve. Obviously, with this thermodynamics data, even nm-sized nanoparticles cannot produce enough surface vacancies. For OER on NiOOH under alkaline conditions, the activity should, therefore, be mainly attributed to the common surface sites without Ni cation vacancies nearby.

5. CONCLUSIONS

This work represents a comprehensive survey of the influence of cationic vacancy on the OER activity at γ-NiOOH, which can be in-situ formed during the self-healing process of NiB_i at appropriate pH values. The enhanced activity can be attributed by the factor at near-neutral pH conditions, the surface of oxides is not stable thermodynamically, and a fraction (4%) of surface cations dissolve into the electrolyte. This process produces surface Ni vacancies dynamically that promote OER on the nearby four-coordinated Ni sites.

Our main results are outlined in the following:

(i) From thermodynamics, the surface Ni cations on γ-NiOOH can be dissolved below the near-neutral pH, while the dissolution of subsurface Ni ions is thermodynamically inhibited.

(ii) On the pristine γ-NiOOH surface, the OER proceeds via the "lattice peroxide" mechanism, that is, $*H_2O \rightarrow *OH \rightarrow *O^{br}OH \rightarrow *O^{br}O \rightarrow O_2$, while on the defective γ-NiOOH surface, the OER proceeds via the "hydroperoxide" mechanism, that is, $*OH + *H_2O \rightarrow *2OH \rightarrow *OOH \rightarrow O_2$

(iii) On the pristine γ-NiOOH surface, the active site is the five-coordinated Ni. The rate-determining step is the first PCET of $*H_2O \rightarrow *O^tH + H^+(aq) + e^-$, with an overpotential of 0.70 V.

(iv) On the defective γ-NiOOH, the OER occurs on a four-coordinated Ni neighboring the cationic vacancy. The rate-determining step is the first PCET of $*H_2O^t \rightarrow *O^tH + H^+(aq) + e^-$. The OER overpotential is reduced substantially to 0.40 V compared with the pristine γ-NiOOH (i.e., 0.70 eV). Such an overpotential drop is

https://dx.doi.org/10.1021/acscatal.9b04975
ACS Catal. 2020, 10, 2581−2590

attributed to the molecule-like geometry of the reactive Ni site, featuring the four-coordinated environment.

■ ASSOCIATED CONTENT

Supporting Information

The Supporting Information is available free of charge at https://pubs.acs.org/doi/10.1021/acscatal.9b04975.

Calculation details for the CHE approach; calculation details for the formation free energy of Ni vacancy; crystal structures for γ-NiOOH; surface energies of γ-NiOOH; and OER profiles on β-NiOOH (PDF)

■ AUTHOR INFORMATION

Corresponding Authors

Ye-Fei Li − *Collaborative Innovation Center of Chemistry for Energy Material, Key Laboratory of Computational Physical Science (Ministry of Education), Shanghai Key Laboratory of Molecular Catalysis and Innovative Materials, Department of Chemistry, Fudan University, Shanghai 200433, China;* orcid.org/0000-0003-4433-7433; Email: yefeil@fudan.edu.cn

Zhi-Pan Liu − *Collaborative Innovation Center of Chemistry for Energy Material, Key Laboratory of Computational Physical Science (Ministry of Education), Shanghai Key Laboratory of Molecular Catalysis and Innovative Materials, Department of Chemistry, Fudan University, Shanghai 200433, China;* orcid.org/0000-0002-2906-5217; Email: zpliu@fudan.edu.cn

Author

Li-Fen Li − *Collaborative Innovation Center of Chemistry for Energy Material, Key Laboratory of Computational Physical Science (Ministry of Education), Shanghai Key Laboratory of Molecular Catalysis and Innovative Materials, Department of Chemistry, Fudan University, Shanghai 200433, China*

Complete contact information is available at: https://pubs.acs.org/10.1021/acscatal.9b04975

Notes

The authors declare no competing financial interest.

■ ACKNOWLEDGMENTS

This work was supported by the National Key Research and Development Program of China (2018YFA0208600), National Science Foundation of China (21773032, 21972023, 21533001, 91545107, 91745201), Science and Technology Commission of Shanghai Municipality (19DZ2270100), Program for Professor of Special Appointment (Eastern Scholar) at Shanghai Institute of Higher Learning.

■ REFERENCES

(1) Friebel, D.; Louie, M. W.; Bajdich, M.; Sanwald, K. E.; Cai, Y.; Wise, A. M.; Cheng, M.-J.; Sokaras, D.; Weng, T.-C.; Alonso-Mori, R.; Davis, R. C.; Bargar, J. R.; Nørskov, J. K.; Nilsson, A.; Bell, A. T. Identification of Highly Active Fe Sites in (Ni,Fe)OOH for Electrocatalytic Water Splitting. *J. Am. Chem. Soc.* **2015**, *137*, 1305−1313.

(2) Yang, C.; Fontaine, O.; Tarascon, J.-M.; Grimaud, A. Chemical Recognition of Active Oxygen Species on the Surface of Oxygen Evolution Reaction Electrocatalysts. *Angew. Chem.* **2017**, *129*, 8778−8782.

(3) Gong, M.; Li, Y.; Wang, H.; Liang, Y.; Wu, J. Z.; Zhou, J.; Wang, J.; Regier, T.; Wei, F.; Dai, H. An Advanced Ni−Fe Layered Double Hydroxide Electrocatalyst for Water Oxidation. *J. Am. Chem. Soc.* **2013**, *135*, 8452−8455.

(4) Smith, R. D. L.; Prévot, M. S.; Fagan, R. D.; Trudel, S.; Berlinguette, C. P. Water Oxidation Catalysis: Electrocatalytic Response to Metal Stoichiometry in Amorphous Metal Oxide Films Containing Iron, Cobalt, and Nickel. *J. Am. Chem. Soc.* **2013**, *135*, 11580−11586.

(5) Trotochaud, L.; Young, S. L.; Ranney, J. K.; Boettcher, S. W. Nickel−Iron Oxyhydroxide Oxygen-Evolution Electrocatalysts: The Role of Intentional and Incidental Iron Incorporation. *J. Am. Chem. Soc.* **2014**, *136*, 6744−6753.

(6) Trotochaud, L.; Ranney, J. K.; Williams, K. N.; Boettcher, S. W. Solution-Cast Metal Oxide Thin Film Electrocatalysts for Oxygen Evolution. *J. Am. Chem. Soc.* **2012**, *134*, 17253−17261.

(7) Lin, C.; Zhao, Y.; Zhang, H.; Xie, S.; Li, Y.-F.; Li, X.; Jiang, Z.; Liu, Z.-P. Accelerated active phase transformation of NiO powered by Pt single atoms for enhanced oxygen evolution reaction. *Chem. Sci.* **2018**, *9*, 6803−6812.

(8) Klaus, S.; Cai, Y.; Louie, M. W.; Trotochaud, L.; Bell, A. T. Effects of Fe Electrolyte Impurities on Ni(OH)2/NiOOH Structure and Oxygen Evolution Activity. *J. Phys. Chem. C* **2015**, *119*, 7243−7254.

(9) Popczun, E. J.; McKone, J. R.; Read, C. G.; Biacchi, A. J.; Wiltrout, A. M.; Lewis, N. S.; Schaak, R. E. Nanostructured Nickel Phosphide as an Electrocatalyst for the Hydrogen Evolution Reaction. *J. Am. Chem. Soc.* **2013**, *135*, 9267−9270.

(10) Saadi, F. H.; Carim, A. I.; Drisdell, W. S.; Gul, S.; Baricuatro, J. H.; Yano, J.; Soriaga, M. P.; Lewis, N. S. Operando Spectroscopic Analysis of CoP Films Electrocatalyzing the Hydrogen-Evolution Reaction. *J. Am. Chem. Soc.* **2017**, *139*, 12927−12930.

(11) Li, Y.; Zhang, L. A.; Qin, Y.; Chu, F.; Kong, Y.; Tao, Y.; Li, Y.; Bu, Y.; Ding, D.; Liu, M. Crystallinity Dependence of Ruthenium Nanocatalyst toward Hydrogen Evolution Reaction. *ACS Catal.* **2018**, *8*, 5714−5720.

(12) Bediako, D. K.; Surendranath, Y.; Nocera, D. G. Mechanistic studies of the oxygen evolution reaction mediated by a nickel−borate thin film electrocatalyst. *J. Am. Chem. Soc.* **2013**, *135*, 3662−3674.

(13) Dinca, M.; Surendranath, Y.; Nocera, D. G. Nickel-borate oxygen-evolving catalyst that functions under benign conditions. *Proc. Natl. Acad. Sci. U.S.A.* **2010**, *107*, 10337.

(14) Bediako, D. K.; Lassalle-Kaiser, B.; Surendranath, Y.; Yano, J.; Yachandra, V. K.; Nocera, D. G. Structure−Activity Correlations in a Nickel−Borate Oxygen Evolution Catalyst. *J. Am. Chem. Soc.* **2012**, *134*, 6801−6809.

(15) Diaz-Morales, O.; Ferrus-Suspedra, D.; Koper, M. T. M. The importance of nickel oxyhydroxide deprotonation on its activity towards electrochemical water oxidation. *Chem. Sci.* **2016**, *7*, 2639−2645.

(16) Lutterman, D. A.; Surendranath, Y.; Nocera, D. G. A Self-Healing Oxygen-Evolving Catalyst. *J. Am. Chem. Soc.* **2009**, *131*, 3838−3839.

(17) Kanan, M. W.; Nocera, D. G. In Situ Formation of an Oxygen-Evolving Catalyst in Neutral Water Containing Phosphate and Co2+. *Science* **2008**, *321*, 1072.

(18) Zhao, Y.; Jia, X.; Chen, G.; Shang, L.; Waterhouse, G. I. N.; Wu, L.-Z.; Tung, C.-H.; O'Hare, D.; Zhang, T. Ultrafine NiO Nanosheets Stabilized by TiO2 from Monolayer NiTi-LDH Precursors: An Active Water Oxidation Electrocatalyst. *J. Am. Chem. Soc.* **2016**, *138*, 6517−6524.

(19) He, Q.; Wan, Y.; Jiang, H.; Pan, Z.; Wu, C.; Wang, M.; Wu, X.; Ye, B.; Ajayan, P. M.; Song, L. Nickel Vacancies Boost Reconstruction in Nickel Hydroxide Electrocatalyst. *ACS Energy Lett.* **2018**, *3*, 1373−1380.

(20) Li, Y.-F.; Selloni, A. Mechanism and Activity of Water Oxidation on Selected Surfaces of Pure and Fe-Doped NiOx. *ACS Catal.* **2014**, *4*, 1148−1153.

(21) Tkalych, A. J.; Zhuang, H. L.; Carter, E. A. A Density Functional + U Assessment of Oxygen Evolution Reaction Mechanisms on β-NiOOH. *ACS Catal.* **2017**, *7*, 5329−5339.

(22) Hareli, C.; Caspary Toroker, M. Water Oxidation Catalysis for NiOOH by a Metropolis Monte Carlo Algorithm. *J. Chem. Theory Comput.* **2018**, *14*, 2380−2385.
(23) Shin, H.; Xiao, H.; Goddard, W. A. In Silico Discovery of New Dopants for Fe-Doped Ni Oxyhydroxide (Ni1−xFexOOH) Catalysts for Oxygen Evolution Reaction. *J. Am. Chem. Soc.* **2018**, *140*, 6745−6748.
(24) Fidelsky, V.; Toroker, M. C. Enhanced Water Oxidation Catalysis of Nickel Oxyhydroxide through the Addition of Vacancies. *J. Phys. Chem. C* **2016**, *120*, 25405−25410.
(25) Martirez, J. M. P.; Carter, E. A. Effects of the Aqueous Environment on the Stability and Chemistry of β-NiOOH Surfaces. *Chem. Mater.* **2018**, *30*, 5205−5219.
(26) Hunter, B. M.; Thompson, N. B.; Müller, A. M.; Rossman, G. R.; Hill, M. G.; Winkler, J. R.; Gray, H. B. Trapping an Iron(VI) Water-Splitting Intermediate in Nonaqueous Media. *Joule* **2018**, *2*, 747−763.
(27) Kresse, G.; Furthmüller, J. Efficient iterative schemes for \textit{ab initio} total-energy calculations using a plane-wave basis set. *Phys. Rev. B: Condens. Matter Mater. Phys.* **1996**, *54*, 11169−11186.
(28) Henkelman, G.; Jónsson, H. A dimer method for finding saddle points on high dimensional potential surfaces using only first derivatives. *J. Chem. Phys.* **1999**, *111*, 7010−7022.
(29) Heyden, A.; Bell, A. T.; Keil, F. J. Efficient methods for finding transition states in chemical reactions: Comparison of improved dimer method and partitioned rational function optimization method. *J. Chem. Phys.* **2005**, *123*, 224101.
(30) Li, Y.-F.; Liu, Z.-P.; Liu, L.; Gao, W. Mechanism and Activity of Photocatalytic Oxygen Evolution on Titania Anatase in Aqueous Surroundings. *J. Am. Chem. Soc.* **2010**, *132*, 13008−13015.
(31) Fattebert, J.-L.; Gygi, F. Density functional theory for efficient ab initio molecular dynamics simulations in solution. *J. Comput. Chem.* **2002**, *23*, 662−666.
(32) Fattebert, J.-L.; Gygi, F. Linear-scaling first-principles molecular dynamics with plane-waves accuracy. *Phys. Rev. B: Condens. Matter Mater. Phys.* **2006**, *73*, 115124.
(33) Fattebert, J.-L.; Gygi, F. First-principles molecular dynamics simulations in a continuum solvent. *Int. J. Quantum Chem.* **2003**, *93*, 139−147.
(34) Perdew, J. P.; Burke, K.; Ernzerhof, M. Generalized Gradient Approximation Made Simple. *Phys. Rev. Lett.* **1996**, *77*, 3865−3868.
(35) Anisimov, V. I.; Zaanen, J.; Andersen, O. K. Band theory and Mott insulators: Hubbard U instead of Stoner I. *Phys. Rev. B: Condens. Matter Mater. Phys.* **1991**, *44*, 943−954.
(36) Zaffran, J.; Caspary Toroker, M. Benchmarking Density Functional Theory Based Methods To Model NiOOH Material Properties: Hubbard and van der Waals Corrections vs Hybrid Functionals. *J. Chem. Theory Comput.* **2016**, *12*, 3807−3812.
(37) Martirez, J. M. P.; Carter, E. A. Unraveling Oxygen Evolution on Iron-Doped β-Nickel Oxyhydroxide: The Key Role of Highly Active Molecular-like Sites. *J. Am. Chem. Soc.* **2019**, *141*, 693−705.
(38) Cococcioni, M.; De Gironcoli, S. Linear Response Approach to the Calculation of the Effective Interaction Parameters in the LDA+ U Method. *Phys. Rev. B: Condens. Matter Mater. Phys.* **2005**, *71*, 035105.
(39) García-Mota, M.; Bajdich, M.; Viswanathan, V.; Vojvodic, A.; Bell, A. T.; Nørskov, J. K. Importance of Correlation in Determining Electrocatalytic Oxygen Evolution Activity on Cobalt Oxides. *J. Phys. Chem. C* **2012**, *116*, 21077−21082.
(40) Li, Y.-F.; Selloni, A. Mosaic Texture and Double c-Axis Periodicity of β-NiOOH: Insights from First-Principles and Genetic Algorithm Calculations. *J. Phys. Chem. Lett.* **2014**, *5*, 3981−3985.
(41) Fang, Y.-H.; Liu, Z.-P. Mechanism and Tafel Lines of Electro-Oxidation of Water to Oxygen on RuO2(110). *J. Am. Chem. Soc.* **2010**, *132*, 18214−18222.
(42) Li, Y.-F.; Liu, Z.-P.; Liu, L.; Gao, W. Mechanism and Activity of Photocatalytic Oxygen Evolution on Titania Anatase in Aqueous Surroundings. *J. Am. Chem. Soc.* **2010**, *132*, 13008−13015.
(43) Li, Y.-F.; Liu, Z.-P. Active Site Revealed for Water Oxidation on Electrochemically Induced δ-MnO2: Role of Spinel-to-Layer Phase Transition. *J. Am. Chem. Soc.* **2018**, *140*, 1783−1792.
(44) Damjanovic, A.; Dey, A.; Bockris, J. O. M. Kinetics of oxygen evolution and dissolution on platinum electrodes. *Electrochim. Acta* **1966**, *11*, 791−814.
(45) Rossmeisl, J.; Qu, Z.-W.; Zhu, H.; Kroes, G.-J.; Nørskov, J. K. Electrolysis of water on oxide surfaces. *J. Electroanal. Chem.* **2007**, *607*, 83−89.
(46) Huang, L.-F.; Hutchison, M. J.; Santucci, R. J., Jr; Scully, J. R.; Rondinelli, J. M. Improved Electrochemical Phase Diagrams from Theory and Experiment: the Ni−water System and its Complex Compounds. *J. Phys. Chem. C* **2017**, *121*, 9782−9789.
(47) Stern, L.-A.; Hu, X. Enhanced oxygen evolution activity by NiOx and Ni(OH)2 nanoparticles. *Faraday Discuss.* **2014**, *176*, 363−379.
(48) Risch, M.; Klingan, K.; Heidkamp, J.; Ehrenberg, D.; Chernev, P.; Zaharieva, I.; Dau, H. Nickel-oxido structure of a water-oxidizing catalyst film. *Chem. Commun.* **2011**, *47*, 11912−11914.
(49) Yoshida, M.; Mitsutomi, Y.; Mineo, T.; Nagasaka, M.; Yuzawa, H.; Kosugi, N.; Kondoh, H. Direct Observation of Active Nickel Oxide Cluster in Nickel−Borate Electrocatalyst for Water Oxidation by In Situ O K-Edge X-ray Absorption Spectroscopy. *J. Phys. Chem. C* **2015**, *119*, 19279−19286.

https://dx.doi.org/10.1021/acscatal.9b04975
ACS Catal. 2020, 10, 2581−2590